DESY Summer Student Programme 2014

Characterization of edgeless sensors

Supervisor: Jiaguo Zhang

Damaris Tartarotti Maimone
Instituto de Física Gleb Wataghin
Universidade Estadual de Campinas
Brazil

Hamburg, DESY
September, 2014

Abstract

Conventional detectors have a relatively large insensitive region. This is due to the presence of current colection ring (CCR) and guard rings (GR) in the sensor, the size of the readout chip and its wire bond connection to the board. This dead region can be extended to few millimeters, depending on the detector. An alternative to reduce the inactive region, or edge, are edgeless detectors. These detectors require a new technology for sensors, ASIC chips with Through-Silicon-Vias (TSV) and Re-Distribution Layer (RDL). The Photon-Science Detector Systems group (FS-DS, DESY) is working on the development of an edgeless LAMBDA (Large Area Medipix Based Detector Array). In this context, it is needed to characterize edgeless sensors.

In this work, we present a characterization of edgeless sensors coupled to conventional Medipix3 chips, which is the chip used in LAMBDA. Three samples were measured, two n-on-p and one n-on-n. The n-on-n sensor could not count photons, and this problem was attributed to a production problem (the backside oxide layer was not fully removed). For the n-on-p sensors, it was possbile to notice that even though these sensors were not fully depleted, they could still be used for imaging experiments. Two equalisation procedures were done for the n-on-p sensor with the CCR , and we could conclude that the equalisation with X-rays is slightly better than the equalisation in dark. For this sample, it was performed a threshold scan in order to measure the X-rays spectrum. From this measurement, it was possbile to observe a distortion in the spectrum, caused by charge sharing.

Contents

1 Introduction and Motivation

A silicon sensor contains a high density of lattice defects in its diced surface. Part of them are eletrically active, leading to a significant leakage current in the device.

To deal with this problem, conventional detectors contains a Current-Collection Ring (CCR) and guard rings. These structures produce an effective screening of the eletric field in the active area from the diced surface, isolating the active area from the dead region, then reducing the leakage current on the pixels of the detector.

However, CCR and guard rings cause conventional detectors have a relatively large insensitive region around their active area. This dead region can be extended to few millimeters, depending on the application of the detector. Furthermore, the practical size of the active area in a detector is limited also by the size of the readout chip and its wire-bond connection to the Low Temperature Co-fired Ceramic (LTCC) board.

An alternative to reduce the edges, i.e. the inactive area, is to use edgeless detectors. These detectors require the implementation of another technology for sensors, the edgeless sensors, compatible with the readout chip. It also requires readout chips with Though-Silicon-Vias (TSV) and Re-Distribution Layer (RDL) implemented, and integration to the LTCC board through Ball-Grid Array (BGA).

Fig. 1 shows cross sections of conventional and edgeless detectors.

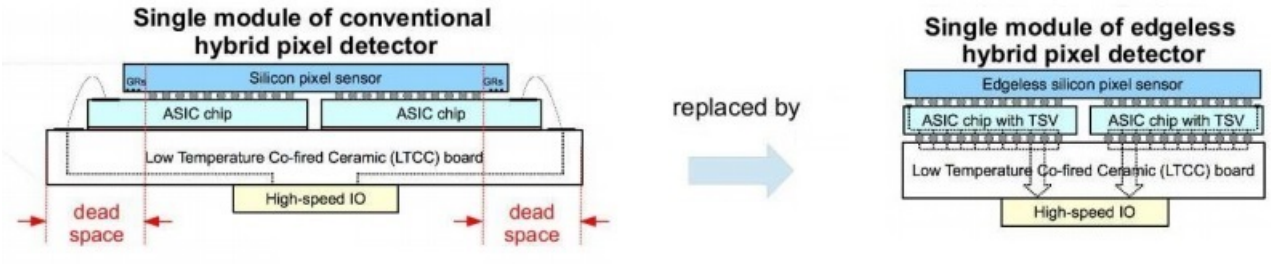

Fig. 1: Cross section of conventional (left) and edgeless detectors (right).

In this work, characterization of edgeless sensors coupled to conventional Medipix3 readout chip will be presented. Medipix3 chip is a readout chip for hybrid pixel detectors. It has been used in the Large Area Medipix-Based Detector Array (LAMBDA), a Photon-Science Detector Systems (FS-DS - DESY) ongoing project.

LAMBDA is a photon-counting pixel detector system developed by DESY, and it presents the problem of large dead region. The dear region is approximately 3.5 mm wide for each module. LAMBDA is based on conventional silicon pixel sensors and Medipix3 readout chip, with a small pixel size of 55μm and high speed, deadtime-free readout. A single LAMBDA module has incorporated 6×2 Medipix3 chips, leading to 1536×512 pixels, and multiple modules can be tiled together to cover a large area. Fig. 2 shows LAMBDA module detector.

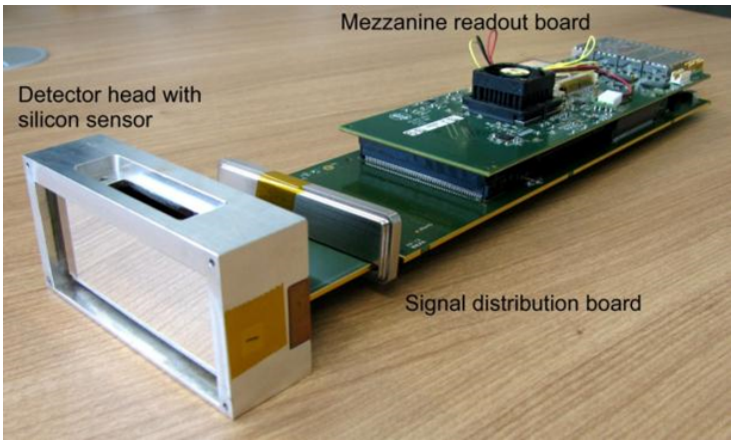

Fig. 2: Single LAMBDA module with 1536 × 512 pixels.

In order to reduce the dead region of current LAMBDA detector, FS-DS group is working on the development of edgeless detector system. Applications based on spectroscopic techniques, like X-ray Fluorescence Spectroscopy (XRF), k-edge imaging as well as time-resolved techniques are some examples of who will benefit from this development.

A lot of efforts have to be put to achieve this goal, and the first steps have already been done by FS-DS. An important step is to perform characterization of the edgeless silicon pixel sensors. For the test of edgeless sensors regarding to the charge-collection of pixels, the sensors have been bump-bonded to Medipix3 readout chip.

The aims of this work are:

- understand the basis of semiconductor physics, sensors and pixel detectors;
- investigate the performance of Si edgeless sensors for 3 different structures.

2 Edgeless sensors and Medipix chips

2.1 Edgeless Sensors

Conventional sensors contains CCR and guard rings. CCR is used to reduce the leakage current procuded by defects locating at the diced edge surface of the silicon sensor. Whereas, guard rings have the function of increasing the breakdown voltage (maximum voltage that can be applied without causing an exponential increase in the current in the silicon sensor). However, CCR and guard rings adds an insensitive area (dead region) close to the sensor's edges.

An alternative to eliminate this dead region and to prevent subsequent leakage current is to use edgeless sensors with active edges. The processes to produce edgeless sensors include a process to create deep penetration on the silicon wafer suffers so-called Deep Reactive Ion Etching (DRIE). After the trench is created, a side implantation of phosporous or boron (n/p-type doping) is done. Furthermore, the processes are done similar to those for a conventional sensor, like Aluminum metallization, passivation on top, backside metalisation etc.

An ideal edgeless sensor should have:

- low leakage current;
- good quantum efficiency;
- high breakdown voltage;
- small last pixel-to-edge distance;
- good sensitivity to low energy photons for edge pixels.

2.2 Medipix Chips

Medipix chips is a family of three generations of readout chips. The first generation, Medipix1 (or Photo Counting Chip - PCC) demonstrated the potential of this technology to provide noise-free single photon counting. The chip consisted of a matrix of 64 $\times$ 64 pixels, and the dimensions of the pixel were 170 μm $\times$ 170 μm. It was implemented in a 1μm CMOS process. The Medipix2 chip was developed with the aim of constructing a sub-micron (0.25 μm) CMOS, and it increased the number of pixels per chip. Also, the dimensions of the pixels in Medipix2 were improved to 55 μm $\times$ 55 μm.

These chips presented a limitation when measuring the energy of a single photon. This technological limitation was realised when measuring a distortion in the energy spectrum by one pixel induced by charge sharing. When the photon comes to the vicinity of the pixel edges, some signal is induced in the neighbouring pixels. The charge generated in a photon interaction is "shared"between pixels. This produces a distortion in the energy spectrum mesured by the pixel. Depending on the threshold programmed in the pixel, the photon can be counted more than once, or the photon can be missed. Furthermore, when using high-Z sensor materials, to increase the quantum efficiency detected at higher photon energies, fluorescence photon can be produced and they deposite their energy at some distance, in an order comparable to the pixel pitch. This can affect the energy spectrum measured by the pixel because part of the energy of the original photon is carried by the fluorescence photon to an adjacent pixel.

The Medipix3 chips were developed to face this problem, permiting imaging in highly segmented hybrid pixel detectors. The distortion in the energy spectrum due to charge sharing in the sensor has been addressed by making adjacent pixels communicate in the analog and digital domains, and then reconstructing event-by-event.

In the first version of Medipix3, the hit allocation mechanism worked poorly because of an unexpectedly high pixel-to-pixel threshold mismatch. The new chip, Medipix3RX implements a new architecture to allocate the hit, improving the performance of the chip.

3 Characterization of edgeless single assembly

3.1 Measured structures

Three samples were measured. First and third structures are n-on-p sensors, while the second is an n-on-n. The difference between the first and third is that the first doesn't have any current-collection ring, while the third does. Comparing the performance of these two structures, it is possible to notice the influence of one CCR in the sensor. All the samples does not have guard rings, characterizing an edgeless sensors. The three Si sensors have a 55μm pitch size, and were coupled to Medipix3 readout chips. The distance from the last electrode on the pixel side to edge was 50 μm for all the three structures. In Tab.1, it is presented the polarity, the thickness, the doping, the depletion voltage and depletion width at its operation votlage for each sensor. The depletion voltage is also given by Eq. 1, and calculated values shown in Tab.1.

$$V_{dep} = \frac{q_0 T_{Si}^2 N_d}{2\epsilon_0 \epsilon_{Si}}, \tag{1}$$

where q_0 is the electron's elementary charge, T_{Si} the sensor's thickness, N_d the doping, ϵ_0 the vacuum permittivity and ϵ_{Si} the Si permittivity.

Characteristics	First Sample	Second Sample	Third Sample
Polarity	n - on - p	n - on - n	n - on - p
Thickness	500 μm	500 μm	500 μm
Doping	1.1 $\times 10^{12} cm^{-3}$	7 $\times 10^{11} cm^{-3}$	1.1 $\times 10^{12} cm^{-3}$
V_{dep}	208.9 V	132.9 V	208.9 V

Tab. 1: Characteristics of measured structures.

Fig. 3 shows cross sections of the three sensors measured.

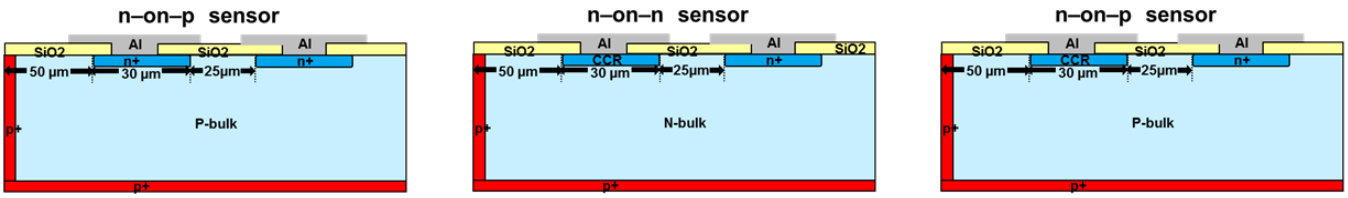

Fig. 3: Cross sections for three measured sensors.

3.2 Measurements

This section describes the measurements performed in order to characterize the samples.

DAC Checking Digital-to-analog converters (DAC) are used to set different analog voltages to the readout chip Medipix3. For Medipix3 chip, it is important to mantain the difference between

V_{CAS} and V_{GND} of $> 150mV$, in order to have the pre-amplifier working properly. There are some optimized values for V_{CAS}, V_{GND} and V_{FBK}. In the Appendix, the values used in measurements after the optimization are given.

I - V measurements By applying a voltage to the sensor and measuring its current, it is possible to determine the breakdown voltage from the Current-Voltage (I-V) curves. To determine which voltage should be applied to the sensor, we have to compare the brakdown voltage with the depletion voltage.

If the breakdown voltage is lower than the depletion voltage , the sensor is judged as a bad sensor.

Equalisation A large pixel to pixel threshold dispersion is observed in Medipix3 readout chip. This has been attributed to transistor thin oxide degradation during the circuit manufacturing. To solve this, each pixels has 5 bits to adjust the threshold. The process of setting these adjustment bits per pixel is called equalisation process. The fabricant C++ routine is used to make the equalisation.

The unequalised Medipix3 has a Gaussian dispersion with a mean roughly at zero. This means that the noise floor of many pixels will not show up in the threshold scan. To shift these pixels so that they are being measured, we can apply the fifth bit. The strength of the shift is called "THRESHOLDN". After the the noisefloor can be measured across all pixels, the remaining 4 bits in each pixel can be used to shift the noisefloor near to zero. The strength of this shift is called "DAC_pixel".

Dark Field Image An image in dark field, that means, with X-rays turned off is taken in order to make a correction for the final images.

Flat Field Image Flat field image refers to an image taken with X-rays uniformly illuminated on the sensor. It is usually used in flat field correction, described below. The X-ray source includes the generator from PANalytical (PW 3830) and a target of Molybdenium. The machine voltage applied was $V_{tube} = 50KV$ and the current $I_{tube} = 40mA$ for most of the following experiments, except for the energy calibration.

Object Image An image is taken with object placed in-between the X-ray source and the edgeless detector. We chose to take the image of a USB flash.

Flat-field Correction The goal of this correction is to remove artifacts in the images caused by variations in the pixel-to-pixel sensitivity of the detector and/or by distortions in the optical path. The flat-field correction is done according to the Eq.2

$$C = \frac{(O - D)m}{F - D}, \tag{2}$$

where C the corrected image, O an object image that is being corrected, D the dark field image, F the flat field image and m the average value of (F - D).

3.3 Results

The results of the measurements are presented in this section, including the I-V characteristics, flat-field images, object images and energy calibration.

3.3.1 I - V curves

From Fig.4, it is possible to determine the breakdown voltage.

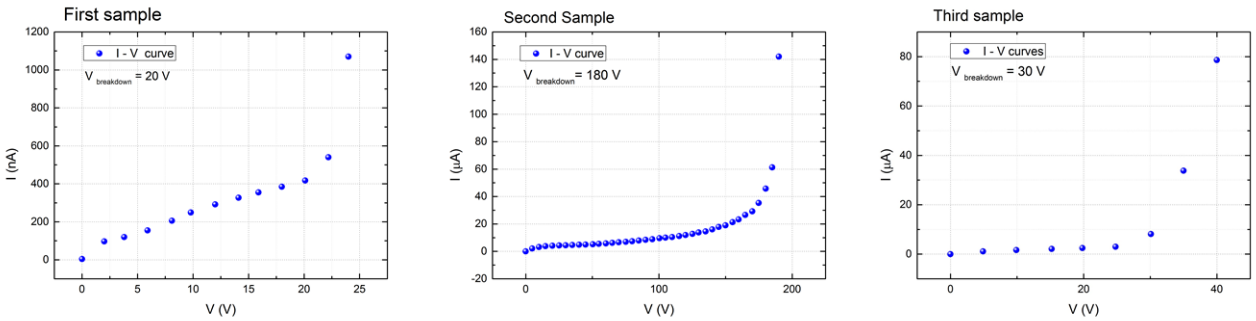

Fig. 4: I - V curves for the three measured samples.

Tab.2 shows a comparison between the breakdown voltage and the depletion voltage, and shows the depletion width, which is given by Eq.3.

$$W_{dep} = \sqrt{\frac{2\epsilon_0 \epsilon_{Si} V_{operation}}{q_0 N_d}}, \tag{3}$$

Voltages	First Sample	Second Sample	Third Sample
V_{dep}	208.9 V	132.9 V	208.9 V
$V_{breakdown}$	22 V	180 V	35 V
$V_{operation}$	20 V	160 V, 170 V, 180 V and 190 V	20 V
W_{dep}	154.7 V	500 V	154.7 V

Tab. 2: Voltages and depletion width for the three samples.

Notice that the fully depletion voltage were not achieved by first and third samples.

3.3.2 Equalisation

The results for Equalisation are shown in Tab.3. For these measurements, the Equalisation was performed in dark environment.

3.3.3 Dark Field Images

Fig.5 shows the dark field images for the three samples. The thresholds for the three samples were 50, 30 and 30. It hardly can be seen photons with these threshold settings. The same settings were used in the flat-field image experiments and images with an object.

Characteristics	First Sample	Second Sample	Third Sample
THRESHOLDN	39	22	38
DAC-pixel	114	92	124
Threshold	50	30	30

Tab. 3: THRESHOLDN, DAC-pixel and Threshold for the three measured samples.

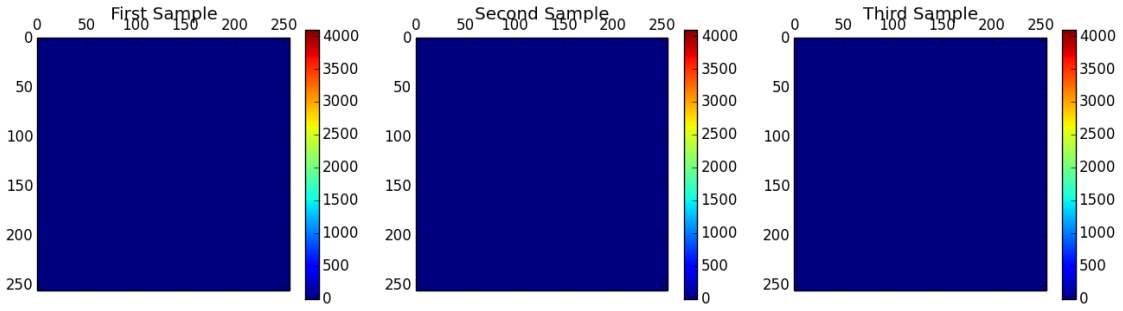

Fig. 5: Dark Field Image for the three samples.

3.3.4 Flat Field Images

Fig.6 shows the flat field images for the three samples. The same threshold settings were used as for dark field images.

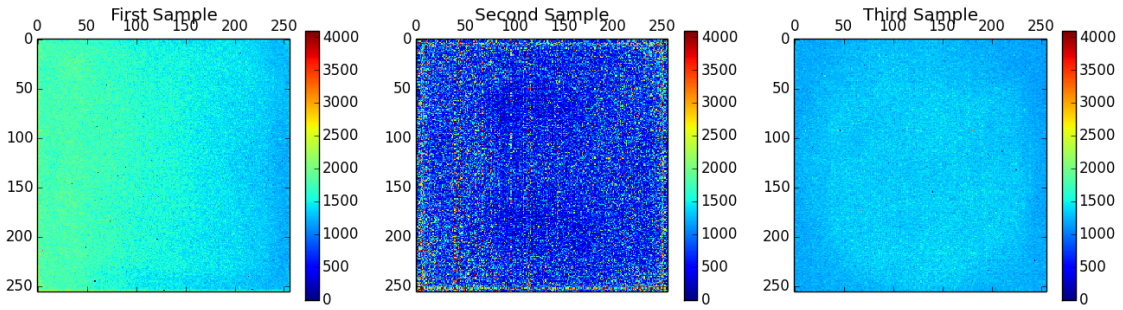

Fig. 6: Flat Field Image for the three samples.

It is noted that the first sample shows a higher counts on the left pixels if compared to the right pixels. This is due to the alignment of the sample to the X-ray beam. In order to make this correction, it is essential perform the flat-field correction.

For the second sample, we see that there is no counts. Four $V_operation$ below the breakdown voltage were used in the measurements, and the results are shown in Fig.7. These operation voltages were not sufficient to make all the pixels functioning. This problem was attributed to a voltage problem intrinsic to the n-on-n sensor. Adivacan (REF), the producer of the sensor, confirmed a problem during the production, that the oxide layer was not fully removed from the backside where X-rays enter.

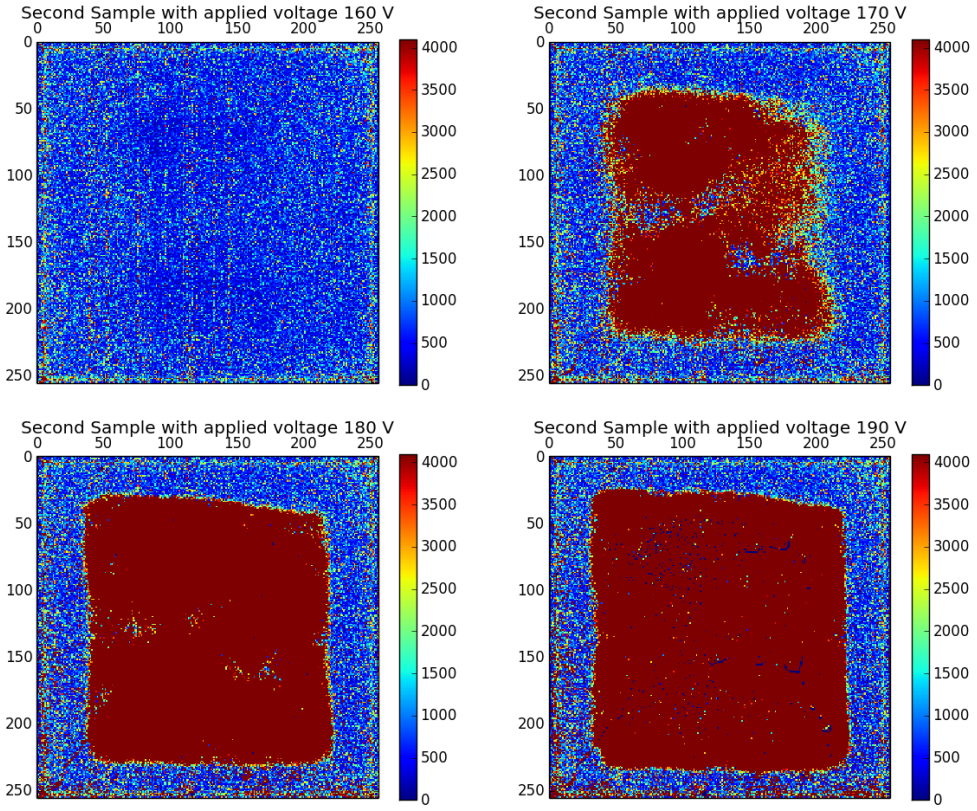

Fig. 7: Flat Field Image for different voltages applied in the second sensor.

Thus, the following imaging measurements with an object were not performed for the second sample.

3.3.5 Object Raw Images and Flat Field Corrected Images

Fig.9 shows the object images for the first and third sample.

From these measurements, it is possible to notice that even the sensors are not fully depleted, they can still work for imaging purposes to certain sense.

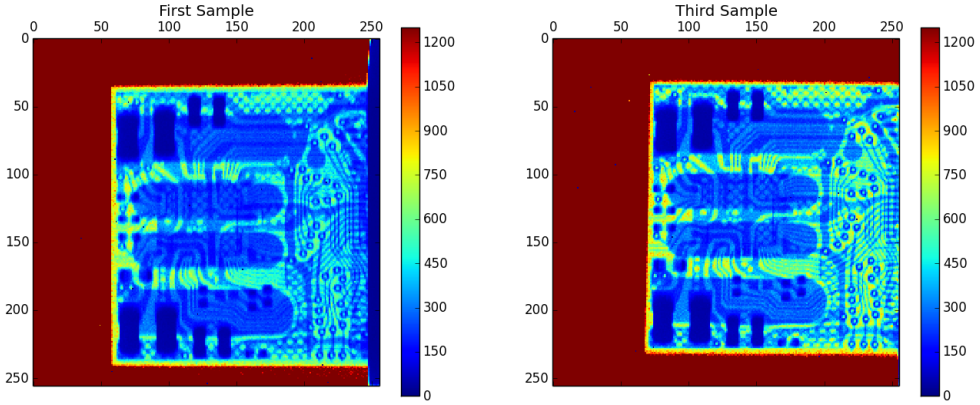

Fig. 8: Object Image of an USB sticker for first and third samples.

Fig.9 shows the object images for the first and third sample after flat field correction.

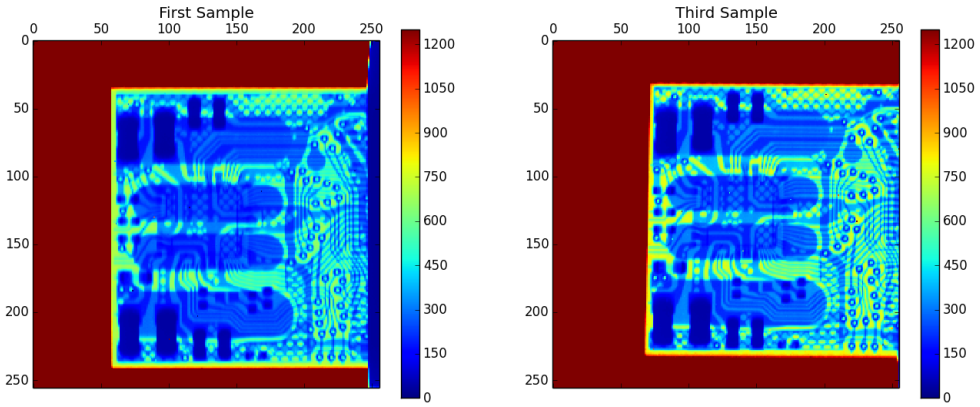

Fig. 9: Object Image of an USB sticker after flatfield correction for first and third samples.

The images get better after flatfield corrected, as expected.

3.3.6 Counts × Pixel and Simulation for the first sample

For the first sample, it is presented a comparison between the results for the "Counts × Pixel number from the edge"and the "Current in the sensor × pixel number from the edge". Fig. 10 shows this comparison.

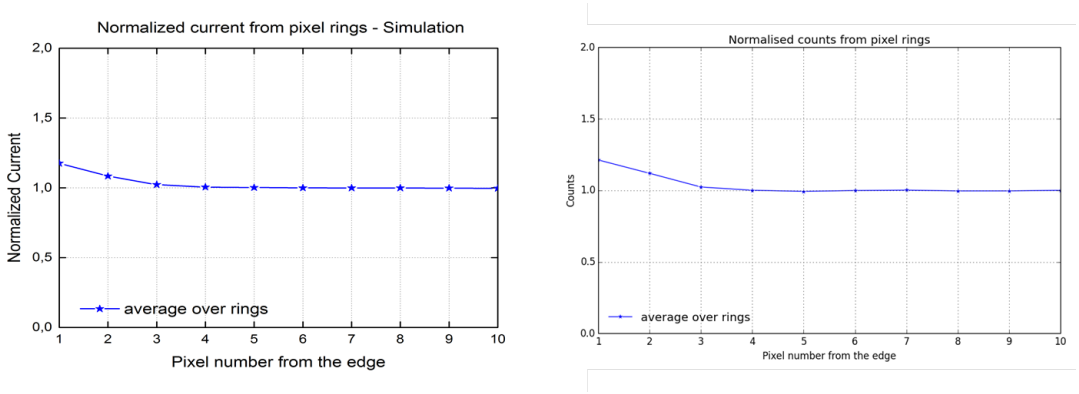

Fig. 10: Results of the simulationurrent in the sensor $\times$ pixel number from the edge (left). Results of the measured counts $\times$ pixel number from the edge (right).

From Fig.10, it is found that the edge pixels count differently from central pixels. This is due to a change on the electric field inside the device. We see also that the simulated current reproduces the measurements results.

A simulation for a good sensor was also performed and the results is shown in Fig.11.

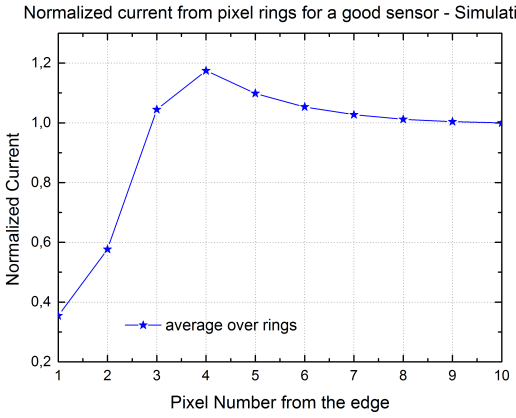

Fig. 11: Results of the simulation current in the sensor $\times$ pixel number from the edge for a good sensor.

The prediction for a good sensor (full depletion) shows that the last few pixels counts much less than central pixels.

3.4 Performance of Equalisation Procedure

In this section, we present the results comparing two different equalisation procedures. One equalisation was done in dark environment, and the other was performed with X-rays turned on.

3.4.1 Threshold Scan in dark environment

Fig.12 shows the results for the Threshold scan in dark environment performed comparing equalisation in dark and equalisation with X-rays.

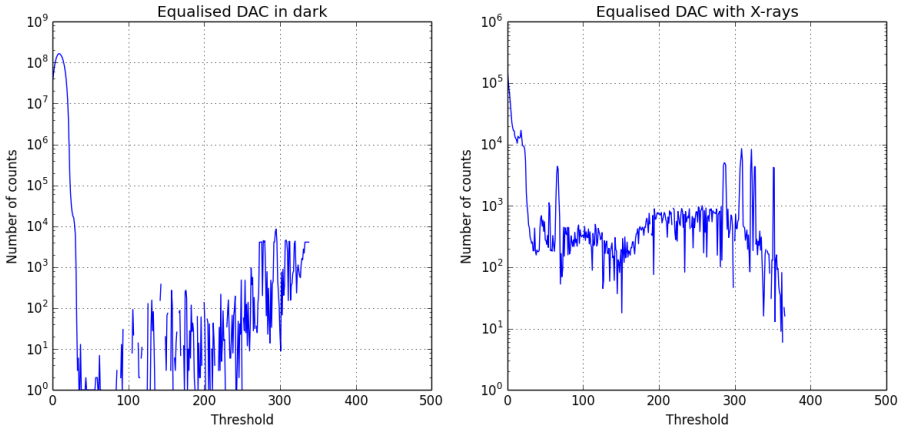

Fig. 12: Threshold scan in dark environment performed with equalisation in dark (left) and equalisation with X-rays (right).

3.4.2 Threshold Scan in X-rays

Fig.13 shows the results for the Threshold scan with X-rays on, comparing equalisation in dark and equalisation with X-rays.

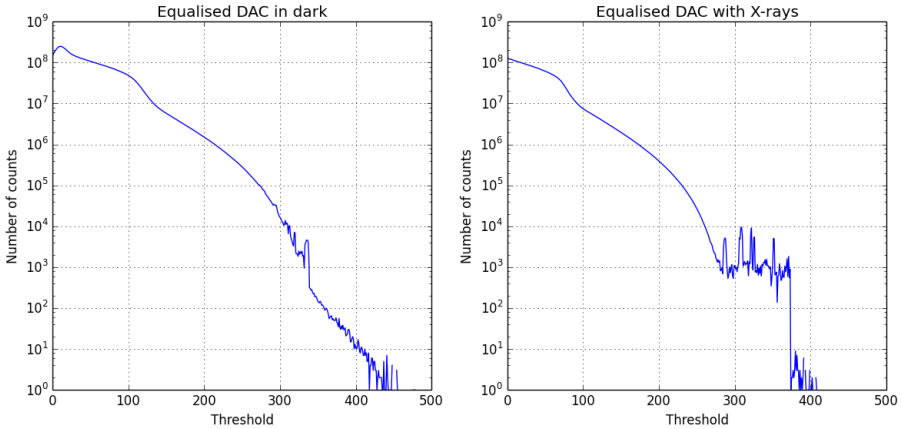

Fig. 13: Threshold scan in x-rays performed with equalisation in dark (left) and equalisation with X-rays (right). The mesurements were performed with $V_{tube} = 50$kV and $I_{tube} = 40$ mA.

3.4.3 Flat Field Image

Fig.14 shows the Flat Field Images comparing the two different equalisation procedures.

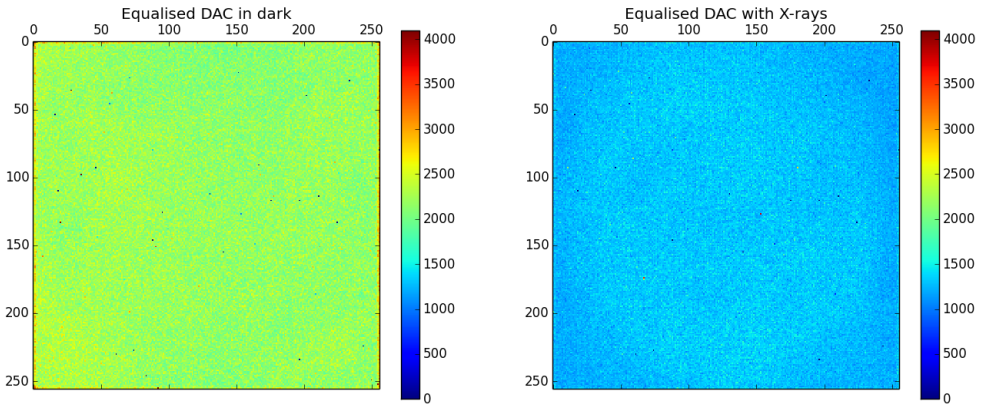

Fig. 14: Flatfield Image performed with equalisation in dark (left) and equalisation with X-rays (right). The mesurements were performed with $V_{tube} = 50$kV and $I_{tube} = 40$ mA.

It is possible to notice that for equalisation performed in dark the counts are higher than for equalisation performed with X-rays on.

3.4.4 3-D Plot

Fig.15 shows the 3-D plot for the counts comparing the two different equalisation procedures.

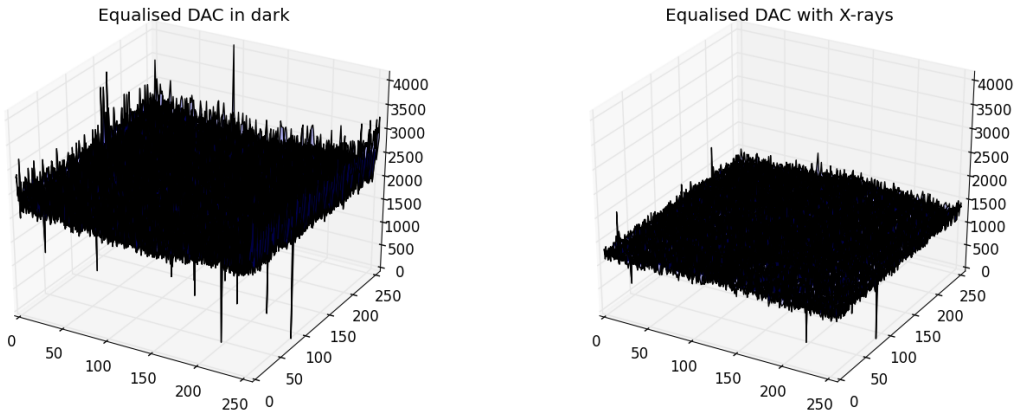

Fig. 15: 3-D plot performed with equalisation in dark (left) and equalisation with X-rays (right). Results from the flat field image.

The statistics and fluctuations of counts for different pixels can be clearly seen.

3.4.5 Number of Pixels $\times$ Counts

Fig.16 shows the "Number of Pixels $\times$ Counts"for the different equalisation procedures.

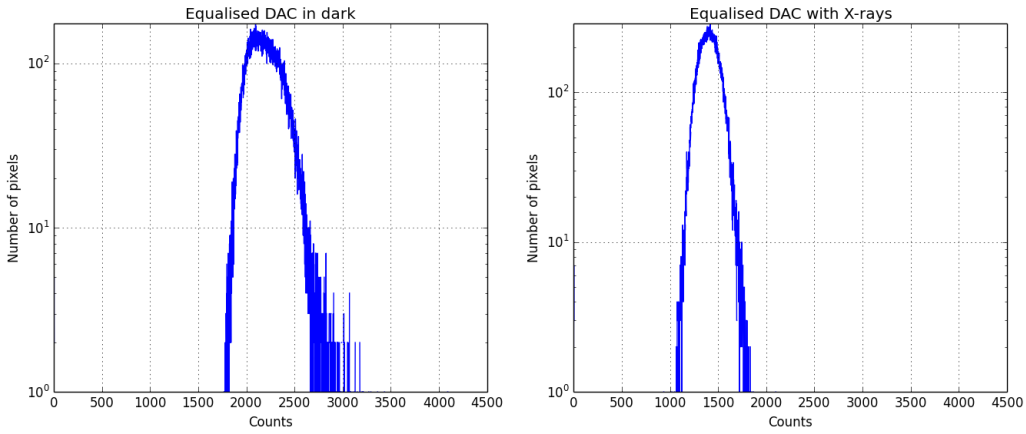

Fig. 16: "Number of Pixels $\times$ Counts"performed with equalisation in dark (left) and equalisation with X-rays (right). Results from the flat field image.

We see that the Full Width of Half Maximum (FWHM) for the equalisation DAC performed with X-rays is smaller than FWHM in dark environment.

3.4.6 Edge counts

Fig.17 shows the Counts as a function of the pixel number from the edge for the different equalisation procedures.

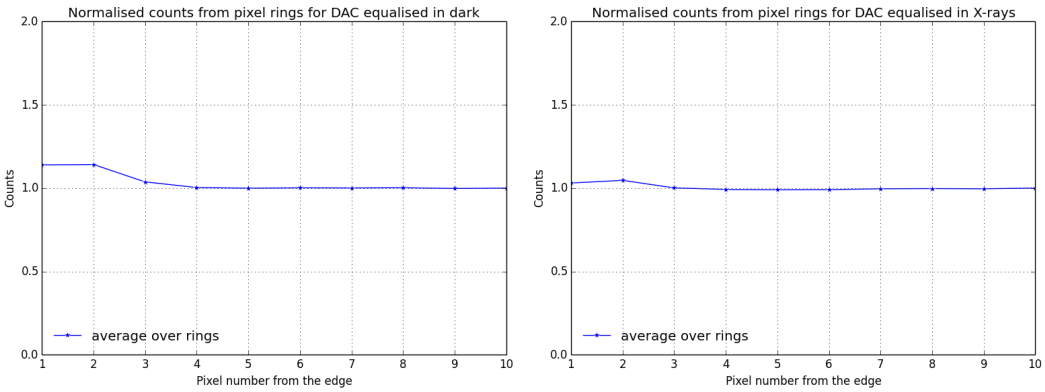

Fig. 17: Counts $\times$ pixel number from the edge with equalisation in dark (left) and equalisation with X-rays (right). Results from the flat field image.

Normalized counts from pixel rings for the two equalisation procedures show a difference of approximately 5%, which means that the difference is not so high between the two different equalisation procedures.

3.4.7 Image of an Object and Image of an Object with Flat Field Correction

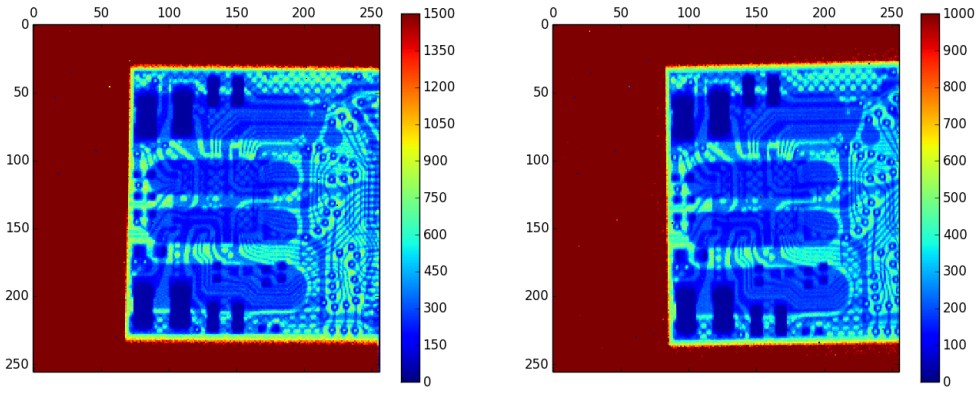

Fig. 18: Image of an object performed with equalisation in dark (left) and equalisation with X-rays (right).

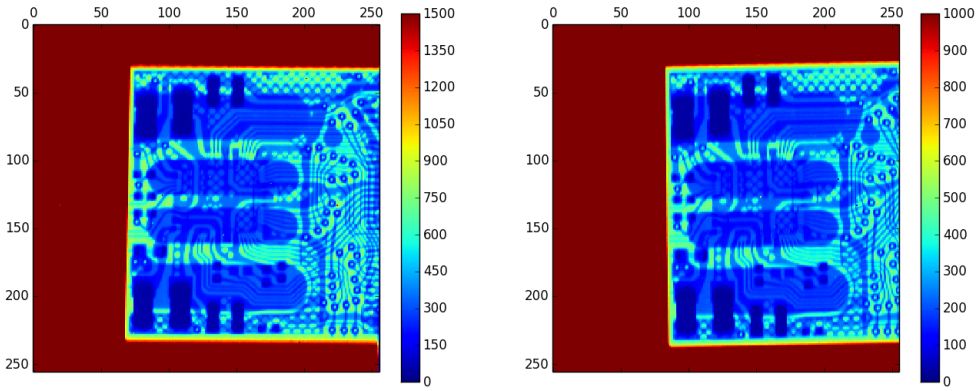

Fig. 19: Image of an objec after flat field correction performed with equalisation in dark (left) and equalisation with X-rays (right).

Object Image for Equalised DAC with X-rays is slightly better than object image for Equalised DAC in dark, but the improvement is not so significant.

3.5 Energy Calibration

Threshold scan selects the energy of the photons to be detected. The starting point of the threshold scan is set above the maximum voltage of the pulse shape distribution, which means that in the beginning of the scan, the detector can not detect any photon. As the threshold voltage is decreasing, when it achieves the maximum voltage of the pulse shape distribution, the detector starts to detect the highests energy photons. Then, the threshold keeps on decreasing, which means that it is detecting not only the highest energy photons, but also photons of lower energy. Measuring the number of photons dependence with threshold number is like to make a scan of the energy spectrum of the X-ray

tube. If one plot the derivative of the number of photons with repect to the threshold as a function of the threshold, it is equivalent to measure the spectrum of X-rays.

To actually measure the spectrum of the X-rays, one has to make a calibration of the Threshold with X-ray energy.

To determine the dependence of the Threshold with energy, we set the tube voltage to four values, and performed a Threshold scan for each tube voltage. The graphs of the "Average counts per pixel $\times$ Threshold"are shown in Fig. 20.

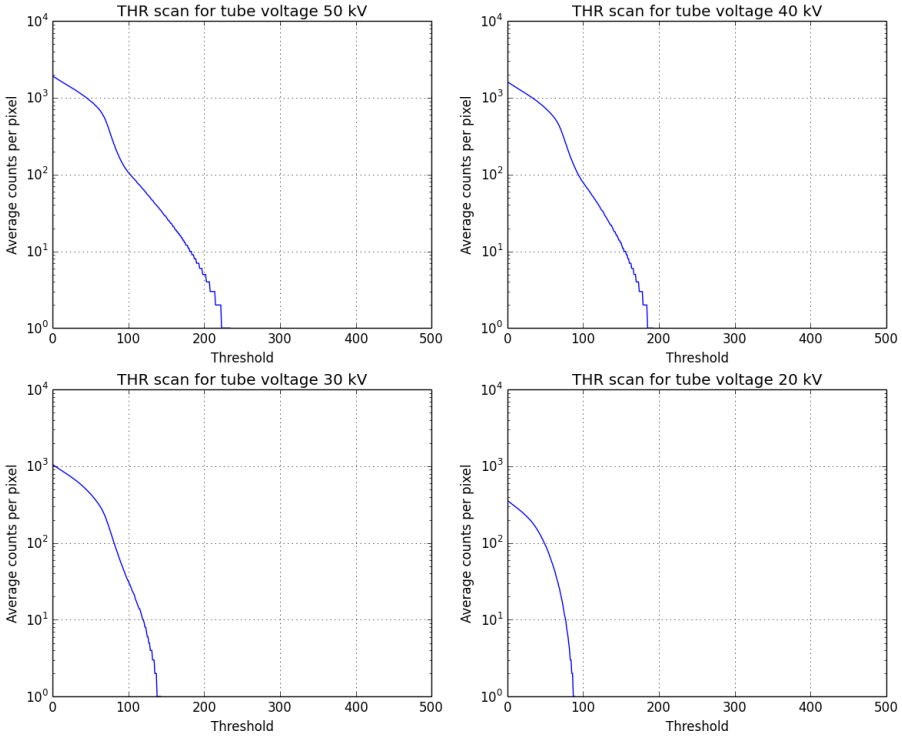

Fig. 20: Average counts per pixel $\times$ Threshold graphs for different voltage

The maximum value of the energy of the photons in each case ($E_{max} = V$, where E_{max} is given in eV and V is the tube voltage) correspond to the threshold intersection with the threshold axis. As the y axis is normalized, instead of a point of intersection, we have a line of threshold giving one count. We chose to stablish the mean value for this point. meanvalue where the Average counts are equal 1.

Then, we can get this value from the curves shown in Fig. 20 and establish the relation between energy and Threshod and make a linear plot to establish the dependence of the Threshold with the Energy. Fig. 21 shows the calibration result.

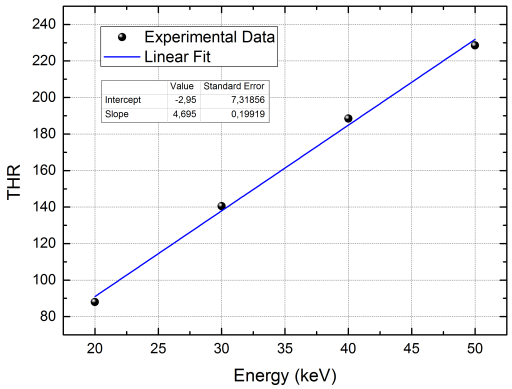

Fig. 21

From this plot, it is possible to establish the relation between the energy and threshold. After that, it is easy to get the spectrum of the X-rays for each tube voltage. This spectrums are shown in Fig. 22.

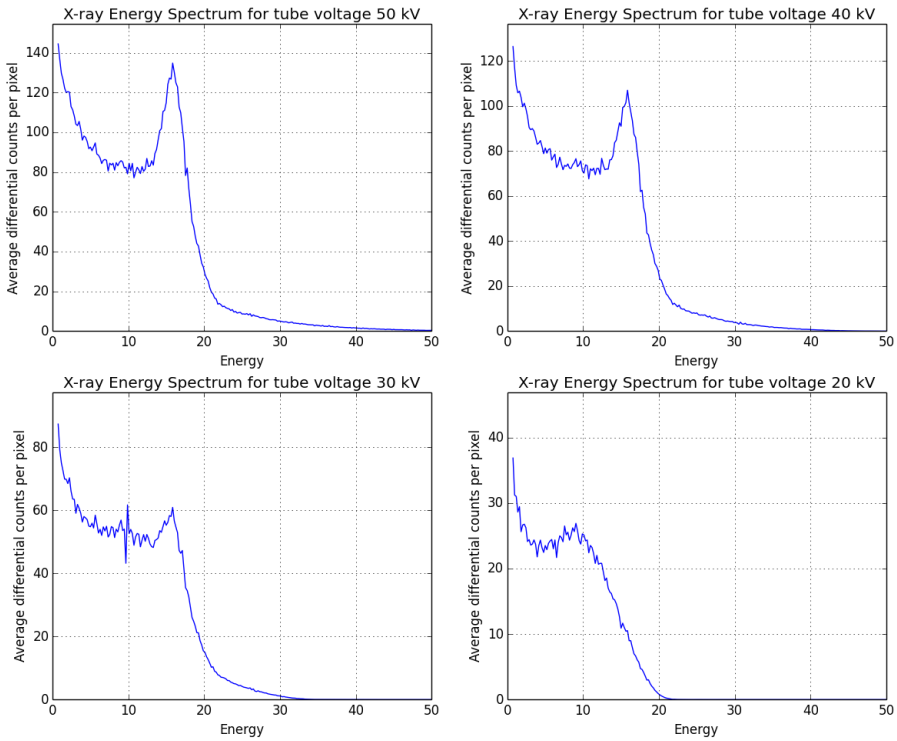

Fig. 22: Spectrums of the X-ray tube for the different tube voltages.

The peak is related to the K-alpha peak. From these measurements, we can see that the peak is located at 16 ± 2 keV.

In the 20 KeV spectrum, we can see a distortion of the spectrum. This is due to the poorly hit allocation mechanism of the first version of Medipix3 discussed in subsection 2.2.

It should be noted that the measured spectrum is not the original spectrum coming out of the X-ray tube, but absorbed spectrum in the silicon sensor with charge sharing effect contributed.

4 Conclusion

By executing this project, it was possible to notice the importance of detectors in Photon Science and more than that, the importance of the development of new technology for detectors. In particular, understanding and investigating the performance of edgeless detectors is of great importance for many applications, like X-ray imaging reconstruction.

In this project, three edgeless samples were tested. The first and the third structures were n+p sensors, and the second was a n+n. From the I-V measurements, we conclude that the breakdown voltage for the first and the third sample could not achieve the full depletion, but they still can be used for imaging experiments. For the n-on-n sensor, we could see that not all the pixels were counting the photons when measuring the the flat field images. This problem was attributed to the process of production, and the vendor (Advacam) confirmed that it was due to backside oxide not completely removed. For the first and third sample, an image of an object (we chose an USB drive) was taken. Both sensors worked, but unfortunately 350 μm could not be depleted.

Normalized counts (charge-collection) from edge pixels understood was taken and compared to I-V simulation results. The simulation shows good agreement to measurement. A prediction for good sensors (which can be fully depleted) was done.

A different equalisation procedure was performed: "Equalisation without X-rays (dark environment) and Equalisation with X-rays."Equalisation with X-rays shows slightly better performance than Equalisation in dark environment.

A measurement of the X-rays Spectrum was also done. It is possible to see a distortion in the energy spectrum, due to charge sharing.

5 Appendix - DAC values Optimized

As mentioned in subsection 3.2, three DAC values were optimized and in this section, we present the results. The measurements were performed for the third sample.

The values set on the chip for FBK, GND and CAS before the optimization were 820 mV, 558 mV and 710 mV, respectively. The Optmized value for FBK must be between 500 mV and 900 mV (closer to 900 if pixels count electrons, and closer to 500 mV if count holes). GND must be closer to 500 mV and CAS must be set to GND value plus 150 mV or more. We set FBK to 852 mV, GND to 625 mV and CAS to 800 mV.

The results for comparison are presented in the following subsections.

The difference between default DAC values and optmized DAC values are not significant.

5.1 Flat Field Image

Fig.23 shows the flat field Image performed with DAC values before optimization and after the optimization.

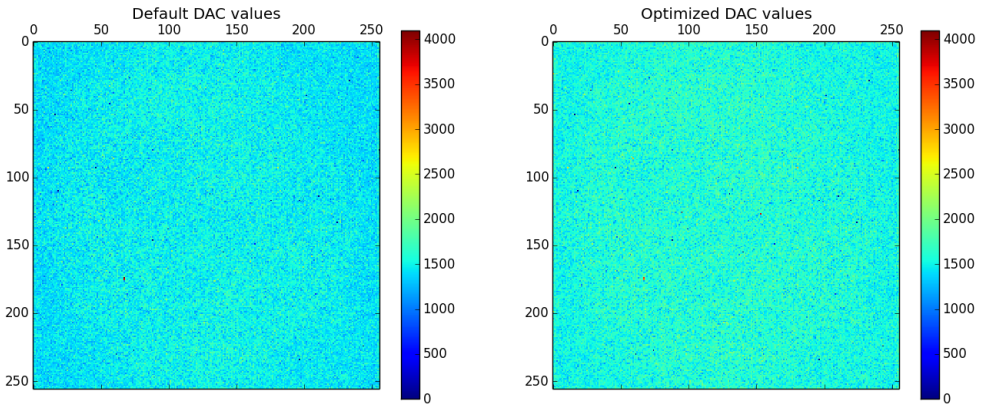

Fig. 23: Flat Field Image performed with DAC values before optimization (left) and after the optimization (right).

5.2 3-D Plot

Fig.24 shows the 3-D Plot performed with DAC values before optimization and after the optimization.

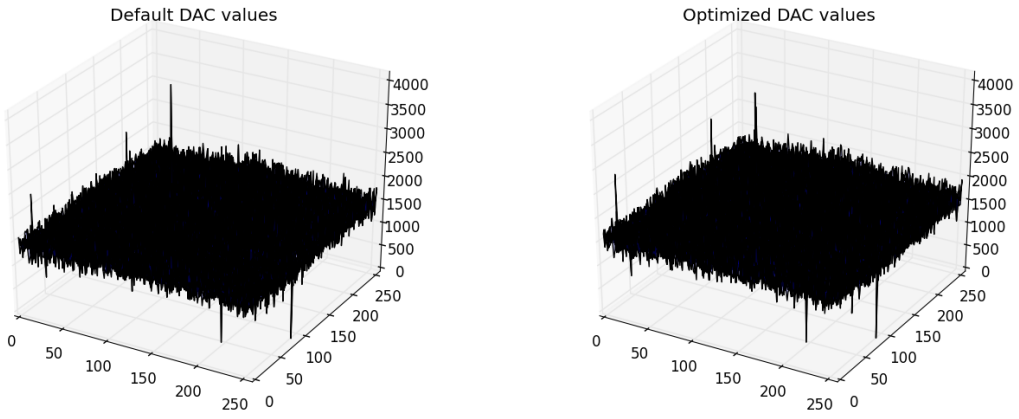

Fig. 24: 3-D Plot performed with DAC values before optimization (left) and after the optimization (right).

5.3 Number of Pixels $\times$ Counts

Fig. 25 shows "Number of Pixels $\times$ Counts"with DAC values before optimization and after the optimization.

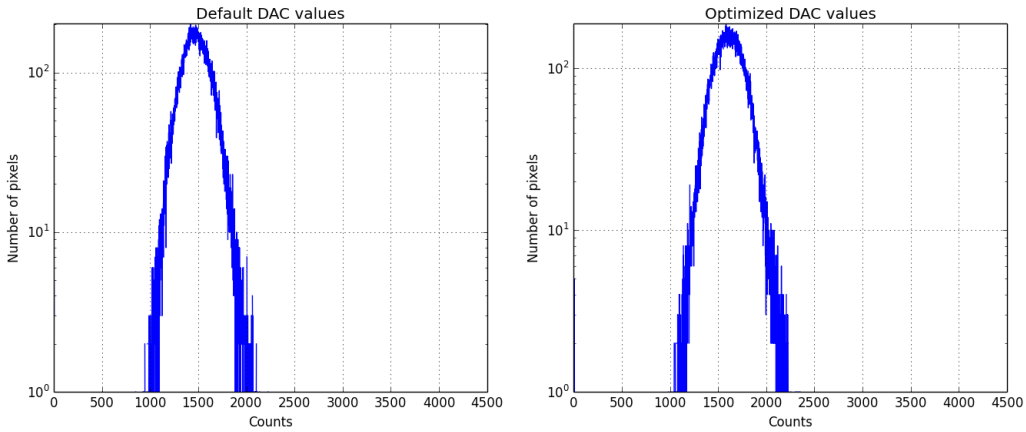

Fig. 25: "Number of Pixels × Counts"with DAC values before optimization (left) and after the optimization (right).

5.4 Edge counts

Fig. 26 shows the counts as a function of the edge pixels for DAC values before and after optmization.

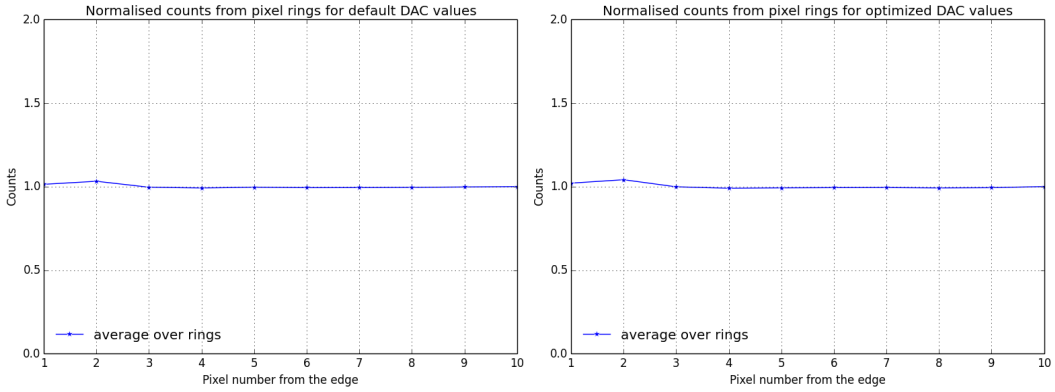

Fig. 26: "Counts × Pixel number from the edge"with DAC values before optimization (left) and after the optimization (right).

6 Bibliography

[1] Pennicard, David, Sabine Lange, Sergej Smoljanin, Julian Becker, Helmut Hirsemann, Michael Epple, e Heinz Graafsma. "Development of LAMBDA: Large Area Medipix-Based Detector Array". Journal of Instrumentation 6, no. 11 (1 de novembro de 2011): C11009. doi:10.1088/1748-0221/6/11/C11009.

[2] Bates, R., A. Blue, M. Christophersen, L. Eklund, S. Ely, V. Fadeyev, E. Gimenez, et al. "Characterisation of Edgeless Technologies for Pixellated and Strip Silicon Detectors with a Micro-Focused X-Ray Beam". Journal of Instrumentation 8, no. 01 (1 de janeiro de 2013): P01018. doi:10.1088/1748-0221/8/01/P01018.

[3] http://www.advacam.com/en/, access on 08/09/2014.

[4] Medipix3 User's Manual.

7 Acknowledgements

I would like to express here my gratitude to my supervisor Jiaguo Zhang, to FS-DS group leader Heinz Graafsma, for giving me the opportunity of working in the FS-DS group during this summer school. I also would like to thank Jiaguo for being helpful and attentive with me.

Furthermore, I would like to thank the organizers of DESY Summer Student Programme in Hamburg 2014, specially Olaf Behnke, Andrea Schrader and Doris Eckstein for providing the conditions to this great time of learning for the summer students.

Thanks for my university "Universidade Estadual de Campinas -UNICAMP"and its Physics Institute "Instituto de Física Gleb Wataghin".

For all the people who worked to give me the opportunity of being in the summer school:

"This summer school was one of the bests experiences in my life. I learned a lot of things, which is what I most seek in life. Not only the topics in the lectures and the contents of the research, I could learn also how you do science here at DESY. I had opportunity to enrich my knowledge it provided me valuable experience for my career. I believe that I evolved a lot during this summer school. Thanks!"